spin momentum, steer axis tilt, and center of mass locations and products of inertia of the front and rear assemblies.

Although we showed that neither front-wheel spin angular momentum nor trail are necessary for self-stability, we do not deny that both are often important contributors. But other parameters are also important, especially the front-assembly mass distribution, and all of the parameters interact in complex ways. As a rule, we have found that almost any self-stable bicycle can be made unstable by misadjusting only the trail, or only the front-wheel gyro, or only the front-assembly center-of-mass position. Conversely, many unstable bicycles can be made stable by appropriately adjusting any one of these three design variables, sometimes in an unusual way. These results hint that the evolutionary, and generally incremental, process that has led to common present bicycle designs might not yet have explored potentially useful regions in design space.

References and Notes

1. W. J. M. Rankine, *The Engineer* **28**, 79 (in five parts) (1869).
2. C. Spencer, *The Modern Bicycle* (Frederick Warne and Co., London, 1876), pp. 23–24.
3. J. P. Meijaard, J. M. Papadopoulos, A. Ruina, A. L. Schwab, http://ecommons.library.cornell.edu/handle/1813/22497 (2011).
4. E. Carvallo, *Théorie du Mouvement du Monocycle et de la Bicyclette* (Gauthier-Villars, Paris, France, 1899).
5. F. J. W. Whipple, *Quarterly Journal of Pure and Applied Mathematics* **30**, 312 (1899).
6. J. P. Meijaard, J. M. Papadopoulos, A. Ruina, A. L. Schwab, *Proc. R. Soc. Lond. A* **463**, 1955 (2007).
7. J. D. G. Kooijman, A. L. Schwab, J. P. Meijaard, *Multibody Syst. Dyn.* **19**, 115 (2008).
8. J. I. Neĭmark, N. A. Fufaev, *Dynamics of Nonholonomic Systems* (Nauka, Moscow, 1967) [J. R. Barbour, transl. (American Mathematical Society, Providence, RI, 1972)].
9. D. E. H. Jones, *Phys. Today* **23**, 34 (1970) [reprinted by *Phys. Today* **59**, 9 (2006), pp. 51–56].
10. K. J. Åström, R. E. Klein, A. Lennartsson, *IEEE Contr. Syst. Mag.* **25**, 26 (2005).
11. F. Klein, A. Sommerfeld, *Über die Theorie des Kreisels* (Teubner, Leipzig, 1910).
12. J. A. Griffiths, *Proc. Inst. Mech. Eng.* **37**, 128 (1886).
13. In the preface to (*11*), the authors credit Fritz Noether for the ideas in the bicycle chapter.
14. W. Thomson, *Popular Lectures and Addresses* (Macmillian, London, 1889), **1**, pp. 142–146.
15. J. M. Papadopoulos, Bicycle steering dynamics and self-stability: A summary report on work in progress (1987), Internal report from the Cornell Bicycle Research Project; available at http://ruina.tam.cornell.edu/research/topics/bicycle_mechanics/bicycle_steering.pdf.
16. E. J. Routh, *Proc. Lond. Math. Soc.* **1**, 97 (1873).
17. R. N. Collins, thesis, University of Wisconsin, Madison, WI (1963).
18. C. Chateau, *La Nature* **20**, 353 (1892).
19. R. S. Hand helped with the theory and experiments; A. Dressel helped with the eigenvalue analysis; J. van Frankenhuyzen helped with designing the experimental machine; and J. Moore helped with conducting the experiments. The manuscript was improved by comments from M. Broide, M. Cook, A. Dressel, J. Guckenheimer, R. Klein, D. Limebeer, C. Miller, J. Moore, R. Pohl, L. Schaffer, and D. van Nouhuys. The research was initially supported by a NSF Presidential Young Investigators award to A.R. The original theory was mostly by J.M.P. with later refinement by A.L.S. J.P.M. found the error in (*11*). Experiments were performed mostly by J.D.G.K. and A.L.S. Writing was done mostly by A.R. and A.L.S.

DNA Origami with Complex Curvatures in Three-Dimensional Space

Dongran Han,[1,2]* Suchetan Pal,[1,2] Jeanette Nangreave,[1,2] Zhengtao Deng,[1,2] Yan Liu,[1,2]* Hao Yan[1,2]*

We present a strategy to design and construct self-assembling DNA nanostructures that define intricate curved surfaces in three-dimensional (3D) space using the DNA origami folding technique. Double-helical DNA is bent to follow the rounded contours of the target object, and potential strand crossovers are subsequently identified. Concentric rings of DNA are used to generate in-plane curvature, constrained to 2D by rationally designed geometries and crossover networks. Out-of-plane curvature is introduced by adjusting the particular position and pattern of crossovers between adjacent DNA double helices, whose conformation often deviates from the natural, B-form twist density. A series of DNA nanostructures with high curvature—such as 2D arrangements of concentric rings and 3D spherical shells, ellipsoidal shells, and a nanoflask—were assembled.

DNA nanotechnology can now be used to assemble nanoscale structures with a variety of geometric shapes (*1–12*) [for a recent review, see (*13*)]. Conventionally, a series of B-form double helices are brought together and arranged with their helical axes parallel to one another. The structure is held together by crossovers between neighboring helices, and the allowed crossover points are based on the pre-existing structural characteristics of B-form DNA. Many DNA nanostructures are variations of polygonal shapes and, although this level of complexity has been sufficient for many purposes, it remains a challenge to mimic the elaborate geom-etries in nature because most biological molecules have globular shapes that contain intricate three-dimensional (3D) curves. Here, we reveal a DNA origami design strategy to engineer complex, arbitrarily shaped 3D DNA nanostructures that have substantial intrinsic curvatures. Our approach does not require strict adherence to conventional design "rules" but instead involves careful consideration of the ideal placement of crossovers and nick points into a conceptually prearranged scaffold to provide a combination of structural flexibility and stability.

The scaffolded DNA origami folding technique, in which numerous short single strands of DNA (staples) are used to direct the folding of a long single strand of DNA (scaffold), is thus far one of the most successful construction methods based on parallel, B-form DNA (*14*). The most commonly used scaffold (M13) is ~7000 nucleotides (nts) long and is routinely used to construct objects with tens to hundreds of nanometer dimensions. Several basic, geometric 3D shapes such as hollow polygons and densely packed cuboids have been demonstrated, as well as a few examples of more complex structures, including a railed bridge and slotted or stacked crosses (*15–17*). The biggest limitation with conventional, block-based DNA origami designs is the level of detail that can be achieved. Analogous to digitally encoded images, DNA origami structures are usually organized in a finite, raster grid, with each square/rectangular unit cell within the grid (pixel) corresponding to a certain length of double-helical DNA. The target shape is achieved by populating the grid with a discrete number of DNA pixels (for most origami structures, each DNA pixel has a parallel orientation with respect to the other pixels) in a pattern that generates the details and curves of the shape. However, as with all finite pixel-based techniques, rounded elements are approximated and intricate details are often lost.

Recently, Shih and co-workers reported an elegant strategy to design and construct relatively complex 3D DNA origami nanostructures that contain various degrees of twist and curvatures (*18*). This strategy uses targeted insertion and deletion of base pairs (bps) in selected segments within a 3D building block (a tightly cross-linked bundle of helices) to induce the desired curvature. Nevertheless, it remains a daunting task to engineer subtle curvatures on a 3D surface. Our goal is to develop design principles that will allow researchers to model arbitrary 3D shapes with control over the degree of surface curvature. In an escape from a rigid lattice model, our versatile strategy begins by defining the desired surface features of a target object with the scaf-

[1]The Biodesign Institute, Arizona State University, Tempe, AZ 85287, USA. [2]Department of Chemistry and Biochemistry, Arizona State University, Tempe, AZ 85287, USA.

*To whom correspondence should be addressed. E-mail: hao.yan@asu.edu (H.Y.); dongran.han@asu.edu (D.H.); yan_liu@asu.edu (Y.L.)

fold, followed by manipulation of DNA conformation and shaping of crossover networks to achieve the design.

First, we designed a series of curved 2D DNA origami structures to establish the basic design principles of our method (*19*). The first step is to create an outline of the desired shape. For illustration purposes, Fig. 1, C and D, show an example shape: a 7-nm-wide concentric ring structure. For this rounded structure, the shape is filled by following the contours of the outline and conceptually "winding" double-helical DNA into concentric rings. The structure is composed of three concentric rings of helices, with an interhelical distance (Δr) of 2.5 nm (from the axial center of one helix to the center of an adjacent helix). This value is based on the observed packing of parallel helices in conventional DNA

origami structures and is merely a first approximation for design purposes (*20*). The circumferences (*c*) of rings are designed to maintain the interhelical distance; therefore, Δc should equal 15.7 nm ($\Delta c = 2\pi \times 2.5$ nm). For B-form DNA, this is equivalent to 48.5 bps, a value that can be adjusted to 48 or 50 bps for ease and symmetry of design. In Fig. 1C, the inner, middle, and outer rings contain 100, 150, and 200 bps, respectively.

The second step is to incorporate a periodic array of crossovers between helices (*19*). Crossovers represent positions at which a strand of DNA following along one ring switches to an adjacent ring, bridging the interhelical gap. Without these crossovers between helices, the rigidity of double-helical DNA (with a persistence length of ~50 nm) (*21*) would cause the DNA in each ring to extend fully. The number and pattern of

crossovers are flexible and will depend on the overall design and on the size of each ring. Theoretically, any divisor of Δc (48 or 50) could be considered; however, a balance between flexibility and structural stability must be maintained. For rings with a Δc of 48 bps, this generally corresponds to 3, 4, 6, or 8 crossovers between helices. For those with a Δc of 50 bps, the number of crossovers should be adjusted to either 5 or 10. These values ensure that the pattern of crossovers is symmetric, with an integer number of bps between sequential crossovers. For helices that are connected to two neighboring rings (this condition applies to all but the inner and outermost rings), the pattern of crossovers must contain nucleotide positions that are facing both of the adjacent helices (tangent). In Fig. 1, the inner/middle and middle/outer rings are connected at five distinct crossover points. Thus, the inner, middle, and outer rings contain 20, 30, and 40 bps between crossovers, which is approximately equal to 2, 3, and 4 full turns (for B-form DNA), respectively. For the middle ring, the alternating crossover points between the inner and outer ring are spaced by 1.5 turns, which ensures that the three rings are approximately in the same plane.
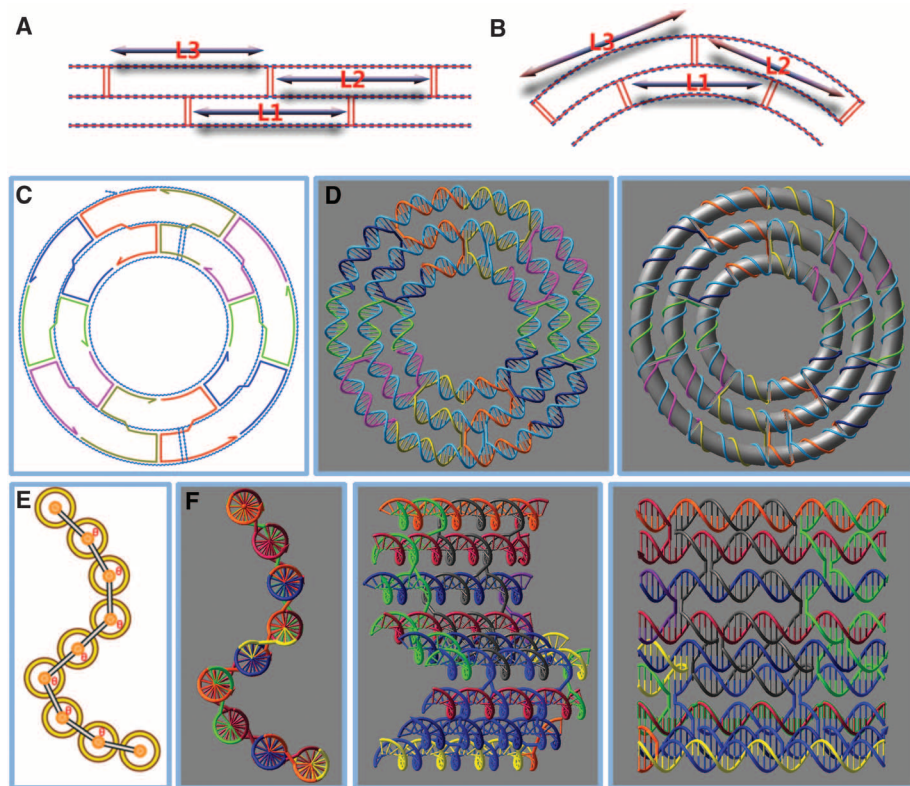

Fig. 1. Design principles for DNA origami with complex curvatures in 3D space. (**A**) A parallel arrangement of DNA double helices to make multihelical DNA nanostructures. The distance between consecutive crossovers connecting adjacent helices (L1, L2, and L3) is constant and generally corresponds to 21 or 32 bps (about two or three full turns of B-form DNA). (**B**) Bending of DNA helices into concentric rings to generate in-plane curvature. The distance between crossovers in the outer rings are greater than in the inner rings (L3 > L2 > L1). This distance is not required to be regular, or exactly equal to a whole number of full turns of B-form DNA for every helix. (**C**) Schematic diagram of a three-ring concentric structure. The long single-stranded DNA scaffold is shown in cyan, and short oligonucleotide staple strands are shown in various colors. Two scaffold crossovers are required between adjacent rings to achieve the three-ring arrangement. They are located far apart, on opposite sides of the rings. Five periodic, staple-strand crossovers connect the outer and middle rings and the middle and inner rings, respectively, constraining the three bent double-helical DNA rings to the same 2D plane. (**D**) Helical and cylindrical view of the three-ring concentric structure. (**E**) A general method to introduce out-of-plane curvature in a multihelical DNA structure. All DNA helices exhibit a natural B-form conformation. There are 10 possible values of θ ranging from ~34° to ~343°. Due to steric hindrance, not all values are allowed. Only a few of these values are demonstrated here. (**F**) Various views of the structure shown in (E), viewed along the helical axes, tilted by 135°, and perpendicular to the helical axes.
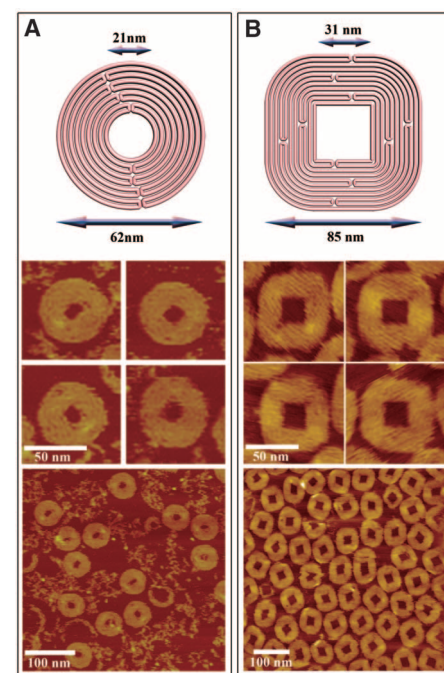

Fig. 2. Curved 2D DNA nanostructures with various structural features. (**Upper panels**) Schematic designs. (**Middle panels**) Zoom-in AFM images with 50-nm scale bars. (**Lower panels**) Zoom-out AFM images with 100-nm scale bars. (**A**) Nine-layer concentric ring structure. Only 3600 of 7249 nucleotides of the scaffold strand are used in this structure, and the remaining single-stranded loop is left unpaired, attached to the outer ring (often visible due to formation of secondary structures). (**B**) Eleven-layer modified concentric square frame structure with rounded outer corners and sharp inner corners.

In the final steps, a long single-stranded scaffold (7249 nts for the typical M13 scaffold, the cyan strands in Fig. 1, C and D) is wound so that it comprises one of the two strands in every helix; each time the scaffold moves from one ring to the next, a "scaffold crossover" is created. Watson-Crick complements to the scaffold (staples, the colored strands in Fig. 1, C and D) are subsequently designed to serve as the second strand in each helix and create the additional crossovers that maintain structural integrity (19). Each staple is generally 16 to 60 nts long and reverses direction after participating in a crossover, resulting in stable antiparallel crossover configurations (5). Once the folding path, crossover pattern, and staple position are determined, a list of staple sequences is generated (19). Several additional factors, including the ideal conformation of DNA double helices, must be considered to complete the design process.

The conformation of each double-helical ring (10 bps/turn) shown in Fig. 1, C and D, closely resembles B-form DNA (10.5 bps/turn), and while the concentric ring structure demonstrates in-plane bending of nonparallel helices, maintaining ~10 bps/turn sacrifices a certain level of design control. For example, sustaining ~10 bps/turn restricts the number of concentric rings that can be added to a structure. As the radius of a ring increases, additional crossover points are required to constrain the double helix to a 2D ring (i.e., 70 bps between crossovers is not expected to maintain the required level of rigidity). Consider adding a fourth, fifth, and sixth ring to the concentric ring structure in Fig. 1, C and D: The fourth ring would have 250 bps with five crossovers (50 bps between crossovers), the fifth ring would have 300 bps with five crossovers (60 bps between crossovers), and, following the same pattern, the sixth ring would have 350 bps with five crossovers (70 bps between crossovers). To stabilize the outer ring would most likely require at least one additional crossover, and the resulting double helix would no longer conform to 10 bps/turn.

DNA has been shown to be flexible enough to tolerate non-natural conformations in certain

DNA nanostructure arrangements (18). To determine the range of DNA conformations amenable to our current design, we constructed a series of three-ring structures (fig. S11) with different numbers of bps between adjacent crossovers and evaluated their stability (19). We found that a wide range of DNA conformations are compatible with DNA origami formation, as confirmed by the atomic force microscopy (AFM) images in fig. S13. As expected, structures in which the DNA most closely resembles its natural conformation (10 and 11 bps/turn) formed with the highest yield (>96%), and those with the largest deviation from 10.5 bps/turn (8 and 13 bps/turn) formed with the lowest yield (fig. S14). The results suggest that it is not necessary to strictly conform to 10.5 bps/turn when designing DNA origami structures, and the flexibility in this design constraint supports more complex design schemes.

With each of these parameters in mind, we designed objects with more complex structural features. Figure 2A illustrates a more intricate concentric ring design, with nine layers of double-helical rings (fig. S26). The design is based on a Δc of 50 bps, and the number of bps/ring ranges from 200 in the innermost to 600 in the outermost ring (with an increment of 50 bps/ring). As the ring size increases, the outer layers need additional crossovers between helices to stabilize the overall structure and preserve the circular shape. The number of crossovers between adjacent helices is five for the two innermost rings, and 10 for the remaining outer rings. Table 1 lists the specific details of each concentric ring layer. The conformation of double-helical DNA in the nine-layer concentric ring structure ranges from 9 to 11.7 bps/turn, with several different distances between successive crossovers. The AFM images in Fig. 2A and fig. S16 reveal that the nine-layer ring structure forms with relatively high yield

(~90%), despite the various degrees of bending in each of the helices and inclusion of non–B-form DNA (19).

A modified square frame (Fig. 2B) was designed to determine whether sharp and rounded elements could be combined in a single structure (figs. S31 to S33). Each side of the modified square frame is based on a conventional helix-parallel design scheme, whereas each corner corresponds to one-fourth of the concentric ring design. The AFM images (Fig. 2B and fig. S18) confirm that several design strategies can in fact be used to generate intricate details within a single structure (19). Several additional 2D designs with various structural features were also constructed (fig. S15). An "opened" version of the nine-layer ring structure was assembled (fig. S27), as well as an unmodified square frame with four well-defined sharp corners (figs. S28 to S30), and a three-point star motif (fig. S34).

To produce a complex 3D object, it is necessary to create curvatures both in and out of the plane. Out-of-plane curvature can be achieved by shifting the relative position of crossover points between DNA double helices (Fig. 1, E and F). Typically, two adjacent B-form helices (n and $n + 1$) are linked by crossovers that are spaced 21 bps apart (exactly two full turns), with the two axes of the helices defining a plane. The crossover pattern of the two-helix bundle and those of a third helix can be offset by any discrete number of individual nucleotides (not equal to any whole number of half turns, which would result in all three helices lying in the same plane), and in this way, the third helix can deviate from the plane of the previous two. However, with B-form DNA, the dihedral angle (θ)—the angle between the planes defined by n and $n + 1$, and $n + 1$ and $n + 2$—can not be finely tuned, and ~34.3°/bp is the smallest increment of curvature that can be achieved.

Table 1. Design parameters for the nine-layer concentric-ring structure. The number of bps in each ring, number of crossovers between adjacent helices, conformation of the double helical DNA in bps/turn, and radius are listed, respectively.

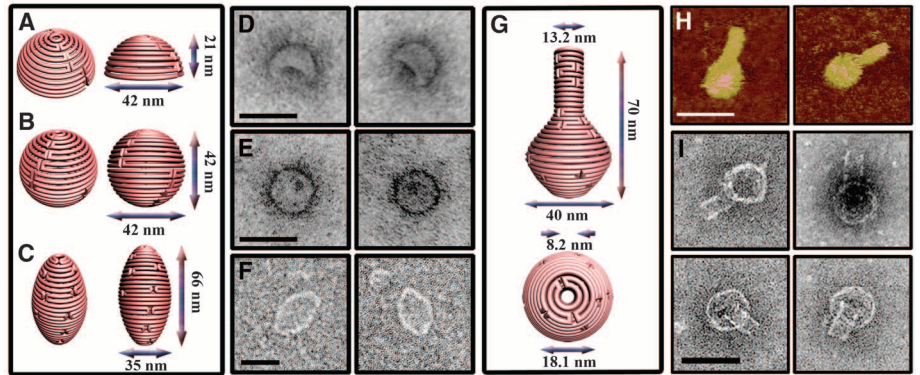| Ring no.	bps	No. of crossovers	bps/turn	Radius (nm)
1	200	5	10	10.3
2	250	5	10	12.9
3	300	10	10	15.5
4	350	10	11.7	18
5	400	10	10	20.6
6	450	10	9	23.2
7	500	10	10	25.8
8	550	10	11	28.4
9	600	–	10	30.9

Fig. 3. DNA nanostructures with complex 3D curvatures. (**A**) Schematic representation of the hemisphere. (**B**) Schematic representation of the sphere. (**C**) Schematic representation of the ellipsoid. (**D**) TEM images of the hemisphere, randomly deposited on TEM grids. The concave surface is visible as a dark area. (**E**) TEM images of the sphere, randomly deposited on TEM grids. Due to the spherical symmetry, the orientation can not be determined. (**F**) TEM images of the ellipsoid. The outline of the ellipsoid is visible. Scale bar for the TEM images in (D), (E) and (F) is 50 nm. (**G**) Schematic representation of the nanoflask. (**H**) AFM images of the nanoflask. Scale bar is 75 nm. (**I**) TEM images of the nanoflask, randomly deposited on TEM grids. The cylindrical neck and rounded bottom of the flask are clearly visible in the images. Scale bar is 50 nm.

The use of non–B-form double-helical parameters presents an opportunity to fine-tune θ. Rationally designed crossover connections between double helices with unique conformations (generally ranging from 9 to 12 bps/turn) provides access to a wide selection of other bending angles between 0 and 360 degrees (tables S5 to S10). Although the extent to which we can manipulate the DNA double helices does not allow us to achieve every angle between 0° and 360°, DNA is flexible enough to approximate the curves found in even the most complex structures.

The design process for a 3D curved object decomposes the object into a wireframe representation (*19*). For example, a sphere would be decomposed just as Earth's surface is divided into latitude circles, which are smaller farther away from the equator (fig. S4). Using a sphere as an example, double-helical DNA is spooled around each latitudinal ring to form a spherical scaffold, starting at the north pole and continuously proceeding from one ring to the next, passing through the equator until finally reaching the south pole. The exact number of latitudinal units (concentric rings) can be varied and will depend on the total length of the available single-stranded DNA scaffold and desired size and diameter of the target object.

The next step is to generate in-plane curvature (latitudinal): i.e., to determine the ideal circumference (in number of bps) of each double-helical ring. When the wireframe is viewed from the top (along the axis defined by connecting the north and south poles), a 2D pattern of concentric circles is observed (fig. S5). Although the center-to-center distance between rings of helices is constant in 3D space, careful inspection of the 2D projection reveals a nontrivial relation between curvature along the latitude and longitude. In the 2D projection, as one moves from the ring corresponding to the north pole out to the equatorial ring, the Δr becomes smaller and smaller. The circumference (in bps) of any initial ring can be randomly defined (based on scaffold length and the desired sphere diameter), and the circumference of each remaining ring is determined by its relation to the initial ring.

After designing latitudinal curvature, out-of-plane (longitudinal) curvature must be introduced. It is helpful to visualize a longitudinal cross section that passes through the north and south poles revealing the helical axis of each latitudinal ring. Now consider only one-half of the cross section (either east or west); starting with ring n (the north pole) and $n + 1$, conceptualize a single plane that passes through the center of both helices. Continue this process and create a plane between $n + 1$ and $n + 2$ and each successive pair of rings until reaching the south pole. It is the total number of latitudinal rings that will determine the dihedral angles between adjacent planes (θ). For example, if a spherical wireframe were constructed from 10 double-helical rings, the angle between adjacent planes would be 162° (180° − 180°/number of rings). The crossover pattern between adjacent helical rings (and position of the nucleotides that participate in each crossover) should be designed to approximate 162° angles.

Finally, a periodic array of crossovers (and staples) is introduced in the same manner and with the same considerations as in the 2D case. The size of each ring dictates the number of crossovers used to maintain overall structural stability and ring shape; the resulting number of bps between crossovers will determine the conformation of the DNA in each ring and, ultimately, the angles available for inducing longitudinal curvature (tables S5 to S10). The in- and out-of-plane curvatures are actually coupled: Modifying the spherical radius and ring circumference will change the number of rings used to generate the sphere (because of the fixed diameter of a DNA double helix); thus, this will change θ. Conversely, adjustments in θ will alter the corresponding radius and circumference. At this point, each curved 3D origami structure must be manually designed, with careful consideration of how to best induce the in- and out-of-plane curvature, the ideal pattern of crossovers, and the appropriate placement and length of staples. Not every value of r and θ is compatible with one another and some cases may require sacrificing control over one parameter or the other to produce the desired structural details. A careful examination of the design schematics for all the reported 2D and 3D objects will provide a better understanding of the design process and the complex relation between r, θ, DNA conformation, crossover pattern, and staple placement. Based on these design principles, we have generated in- and out-of-plane curvature and created several examples of complex 3D DNA architectures, including a hemisphere, a sphere, an ellipsoidal shell, and a "rounded-bottom nanoflask" (Fig. 3).

The hemisphere shown in Fig. 3A contains 12 concentric latitudinal rings with diameters ranging from 5.6 nm at the north pole to 42.0 nm at the equator (fig. S35). θ is a constant 172.5° along the entire surface. The most obvious feature of the hemisphere that can be identified in the transmission electron microscopy (TEM) images in Fig. 3D and fig. S21 is the boundary of the equatorial rings, with the observed diameter of the equator in agreement with the expected value of 42.0 nm (*19*). Notably, the hollow cavity of the hemisphere can sometimes be seen in the TEM images (when it has been randomly deposited on the grid with a tilt) shown in Fig. 3D, providing evidence of its 3D structure.

The full sphere illustrated in Fig. 3B is composed of 24 rings and is an extension of the hemisphere design (fig. S35). Similar to the hemisphere, the diameter of the rings range from 5.6 nm at the north and south poles to 42.0 nm at the equator, and θ (172.5°) is constant along the entire surface. Spherical objects can be seen in the TEM images shown in Fig. 3E and fig. S20, each with the expected diameter of ~40 nm (*19*). The uniformity in the appearance of each ring in the TEM images suggests that the expected 3D sphere successfully formed. If the structure had not assembled as designed, we would likely see variations of partially formed rings, or even rings of several different diameters. A full description of the design details for the sphere and hemisphere (rings 1 to 12) is shown in table S4.

Although the sphere and hemisphere structures demonstrate the ability of our method to produce 3D structures with varying latitudinal curvature (radii) and constant longitudinal curvature (θ), the ellipsoid shown in Fig. 3C tests our ability to create structures with simultaneously shifting radii and θ (fig. S36). This is important because the ability to gradually change the in- and out-of-plane curvature within a single structure is necessary to construct DNA nanostructures with more complicated designs. The ellipsoid contains 29 rings with diameters ranging from 9.8 nm at the poles to 34.6 nm at the equator (table S4). θ is smaller near the poles (severe curvature) and larger at the equator (gradual curvature). The TEM images in Fig. 3F and fig. S22 confirm the successful formation of the ellipsoid structure and provide further evidence of the utility of our method (*19*).

As a final demonstration, we sought to construct an asymmetric object with simultaneously shifting radii and θ. The "nanoflask" shown in Fig. 3G reflects the level of complexity that is found in most natural (e.g., phage virus particles) and non-natural objects (fig. S37). The flask consists of 35 concentric double-helical DNA rings (table S4). The rings that make up the neck of the flask have a constant diameter of 13.2 nm, whereas the round bottom is composed of several different ring sizes, with a diameter of 40 nm at the widest point. θ is a constant 180° in the neck and varies from 160° at the widest point in the round bottom to a maximum of 230° at the junction between the neck and the bottom. The AFM images in Fig. 3H, and TEM images in Fig. 3I and fig. S23, provide evidence of the successful formation of the nanoflasks (*19*). A clear outline of the flask is visible in the TEM images, emphasizing the 3D structural contours; the rounded bottom and the cylindrical neck can be clearly distinguished with the expected dimensions.

The method presented here is fairly easy to execute with comparable yield to the conventional scaffolded DNA origami method. However, for the technique to realize its full potential, several challenges need to be addressed. First, as with conventional DNA origami, the availability of diverse single-stranded scaffolds is limited. Ideally, if longer scaffold alternatives could be identified, larger objects with more complicated features could be constructed. Another important ongoing aim is to develop automated software to aid in the design process. At this point, manual consideration of the complex relations among the design parameters is the most time-consuming step and requires a substantial understanding of fundamental engineering principles and the behavior of interconnected DNA. Despite these future challenges, the current strategy improves our

ability to control the intricate structure of DNA nano-architectures and create more diverse building blocks for molecular engineering.

References and Notes

1. N. C. Seeman, *J. Theor. Biol.* **99**, 237 (1982).
2. N. C. Seeman, *Nature* **421**, 427 (2003).
3. T. J. Fu, N. C. Seeman, *Biochemistry* **32**, 3211 (1993).
4. J. H. Chen, N. C. Seeman, *Nature* **350**, 631 (1991).
5. E. Winfree, F. Liu, L. A. Wenzler, N. C. Seeman, *Nature* **394**, 539 (1998).
6. H. Yan, S. H. Park, G. Finkelstein, J. H. Reif, T. H. LaBean, *Science* **301**, 1882 (2003).
7. W. M. Shih, J. D. Quispe, G. F. Joyce, *Nature* **427**, 618 (2004).
8. F. Mathieu *et al.*, *Nano Lett.* **5**, 661 (2005).
9. R. P. Goodman *et al.*, *Science* **310**, 1661 (2005).
10. F. A. Aldaye, H. F. Sleiman, *J. Am. Chem. Soc.* **129**, 13376 (2007).
11. Y. He *et al.*, *Nature* **452**, 198 (2008).
12. C. Zhang *et al.*, *Proc. Natl. Acad. Sci. U.S.A.* **105**, 10665 (2008).
13. C. Lin, Y. Liu, H. Yan, *Biochemistry* **48**, 1663 (2009).
14. P. W. K. Rothemund, *Nature* **440**, 297 (2006).
15. E. S. Andersen *et al.*, *Nature* **459**, 73 (2009).
16. S. M. Douglas *et al.*, *Nature* **459**, 414 (2009).
17. Y. Ke *et al.*, *J. Am. Chem. Soc.* **131**, 15903 (2009).
18. H. Dietz, S. M. Douglas, W. M. Shih, *Science* **325**, 725 (2009).
19. Materials and methods are available as supporting material on *Science* Online.
20. P. W. K. Rothemund *et al.*, *J. Am. Chem. Soc.* **126**, 16344 (2004).
21. P. J. Hagerman, *Annu. Rev. Biophys. Chem.* **17**, 265 (1988).

Phonemic Diversity Supports a Serial Founder Effect Model of Language Expansion from Africa

Quentin D. Atkinson[1,2]*

Human genetic and phenotypic diversity declines with distance from Africa, as predicted by a serial founder effect in which successive population bottlenecks during range expansion progressively reduce diversity, underpinning support for an African origin of modern humans. Recent work suggests that a similar founder effect may operate on human culture and language. Here I show that the number of phonemes used in a global sample of 504 languages is also clinal and fits a serial founder–effect model of expansion from an inferred origin in Africa. This result, which is not explained by more recent demographic history, local language diversity, or statistical non-independence within language families, points to parallel mechanisms shaping genetic and linguistic diversity and supports an African origin of modern human languages.

The number of phonemes—perceptually distinct units of sound that differentiate words—in a language is positively correlated with the size of its speaker population (*1*) in such a way that small populations have fewer phonemes. Languages continually gain and lose phonemes because of stochastic processes (*2*, *3*). If phoneme distinctions are more likely to be lost in small founder populations, then a succession of founder events during range expansion should progressively reduce phonemic diversity with increasing distance from the point of origin, paralleling the serial founder effect observed in population genetics (*4*–*9*). A founder effect has already been used to explain patterns of variation in other cultural replicators, including human material culture (*10*–*13*) and birdsong (*14*). A range of possible mechanisms (*15*) predicts similar dynamics governing the evolution of phonemes (*11*, *16*) and language generally (*17*–*20*). This raises the possibility that the serial founder–effect model used to trace our genetic origins to a recent expansion from Africa (*4*–*9*) could also be applied to global phonemic diversity to investigate the origin and expansion of modern human languages. Here I examine geographic variation in phoneme inventory size using data on vowel, consonant, and tone inventories taken from 504 languages in the World Atlas of Language Structures (WALS) (*21*), together with information on language location, taxonomic affiliation, and speaker demography (Fig. 1 and table S1) (*15*).

Consistent with previous work (*1*), speaker population size is a significant predictor of phonemic diversity (Pearson's correlation $r = 0.385$, df = 503, $P < 0.001$), with smaller population size predicting smaller overall phoneme inventories (fig. S1A). The same relationship holds for vowel ($r = 0.378$, df = 503, $P < 0.001$) and tone ($r = 0.230$, df = 503, $P < 0.001$) inventories separately, with a weaker, though still significant, effect of population size on consonant diversity ($r =$ 0.131, df = 503, $P = 0.003$). To account for any non-independence within language families, the analysis was repeated, first using mean values at the language family level (table S2) and then using a hierarchical linear regression framework to model nested dependencies in variation at the family, subfamily, and genus levels (*15*). These analyses confirm that, consistent with a founder effect model, smaller population size predicts reduced phoneme inventory size both between families (family-level analysis $r = 0.468$, df = 49, $P < 0.001$; fig. S1B) and within families, controlling for taxonomic affiliation {hierarchical linear model: fixed-effect coefficient (β) = 0.0338 to 0.0985 [95% highest posterior density (HPD)], $P = 0.009$}.

Figure 1B shows clear regional differences in phonemic diversity, with the largest phoneme inventories in Africa and the smallest in South America and Oceania. A series of linear regressions was used to predict phoneme inventory size from the log of speaker population size and distance from 2560 potential origin locations around the world (*15*). Incorporating modern speaker population size into the model controls for geographic patterning in population size and means that the analysis is conservative about the amount of variation attributed to ancient demography. Model fit was evaluated with the Bayesian information criterion (BIC) (*22*). Following previous work (*5*, *6*), the set of origin locations within four BIC units of the best-fit location was taken to be the most likely area of origin under a serial founder–effect model.

The origin locations producing the strongest decline in phonemic diversity and best-fit model lie across central and southern Africa (Fig. 2A). This region could represent either a single origin for modern languages or the main origin under a polygenesis scenario. The best-fit model incorporating population size and distance from the origin explains 31% of the variance in phoneme inventory size [correlation coefficient (R) = 0.558, $F_{2,501} = 113.463$, $P < 0.001$] (Fig. 3). Both population size ($r_{population} = 0.146$, $P = 0.002$)

[1]Department of Psychology, University of Auckland, Private Bag 92019, Auckland, New Zealand. [2]Institute of Cognitive and Evolutionary Anthropology, University of Oxford, 64 Banbury Road, Oxford OX2 6PN, UK.

*E-mail: q.atkinson@auckland.ac.nz

DNA Origami with Complex Curvatures in Three-Dimensional Space

Dongran Han, Suchetan Pal, Jeanette Nangreave, Zhengtao Deng, Yan Liu, and Hao Yan

Use of this article is subject to the Terms of service